INL/JOU-22-68523-Revision-0

Multiaxial Plastic Deformation of Zircaloy-4 Nuclear Fuel Cladding Tubes

February 2023

David W Kamerman, Malachi Michael Nelson

INL/JOU-22-68523-Revision-0

Multiaxial Plastic Deformation of Zircaloy-4 Nuclear Fuel Cladding Tubes

David W Kamerman, Malachi Michael Nelson

February 2023

Idaho National Laboratory
Idaho Falls, Idaho 83415

http://www.inl.gov

Prepared for the
U.S. Department of Energy
Under DOE Idaho Operations Office
Contract DE-AC07-05ID14517

Multi-Axial Plastic Deformation of Zircaloy-4 Nuclear Fuel Cladding Tubes

David Kamerman* – ORCID: 0000-0002-2610-038X – David.Kamerman@inl.gov

Malachi Nelson*+ – ORCID: 0000-0002-6027-552X – Malchi.Nelson@inl.gov

**Idaho National Laboratory, 2525 N. Fremont Ave, Idaho Falls, Idaho 83415*

+ *University of California at Berkeley, 2200 University Ave, Berkeley, California 94704*

Corresponding Author:

David Kamerman

Idaho National Laboratory, 2525 N. Fremont Ave,

P.O. Box 1625, MS 3840, Idaho Falls, Idaho 83415

Phone: (208) 270-3321, Email: David.Kamerman@inl.gov

ABSTRACT

The following work is motivated by the desire to devise an internal pressure test that can mimic a displacement-controlled loading scenario and demonstrate how to apply the multi-axial stress and strain data from the test to develop an elastic/plastic constitutive model for a thin-walled tubular component. This is achieved by conducting simultaneous measurements of tangential and axial strain during the pressure test and integrating these strain measures into a feedback loop with the pressure controller. It is shown how data from such a test can be used to develop a large mechanical property data set relevant to biaxial loading conditions. The data obtained have high confidence evidenced by their low variability and alignment with other literature studies. Additionally, data from these internal pressure tests combined with full-tube axial tensile tests allows for the derivation of the Hill anisotropic yield function. The developed Hill yield function is validated by comparing the plastic strain ratios from the full tube tension tests and by comparing the predicted yield stress in the tangential direction with measured values from ring tension tests in a previous study.

KEYWORDS

Zircaloy; Nuclear Fuel Cladding; Reactivity Initiated Accident; Multi-Axial Deformation;

I. Background and Motivation

During reactor overpower transients, light-water reactor (LWR) fuel cladding is subjected to a multi-axial tensile loading from increasing rod internal pressure due to fission gas and as the result of pellet cladding interaction (PCI). These loads can exceed the cladding yield limits resulting in plastic deformation at high wall stresses. These high, multi-axial stress fields have the potential to cause stress fractures in the cladding. An evaluation of cladding performance in these transients requires development of a stress/strain constitutive model in both the elastic and plastic deformation regimes, which is valid for multi-axial loadings. Zirconium alloy cladding tubes commonly used in the LWRs display anisotropic yield behavior because of their unique crystallographic texture in which hexagonal close packed (HCP) basal poles in HCP crystals are aligned in the radial direction [1]. This texture is one that resists wall thinning [2] often resulting in axial deformation to accommodate changes in diameter. Constitutive models based on data from uniaxial tension tests have the potential to under predict the wall stresses during displacement controlled multi-axial yielding. In uniaxial tension tests, crystal slip can occur early on the most favorable crystallographic planes. In multi-axial loading scenarios, plastic deformation along these favorable slip planes may be inhibited due to an orthogonal constraining force. For thin-walled cladding tubes subjected to loading from either internal pressure or an expanding ceramic pellet, the principal loads are in the tangential and axial directions with an axial to tangential loading ratio of 0.5 (for internal pressure loadings), and between 0.5 and 1 (for PCI loadings depending on the degree of surface slip) [3]. This multi-axial stress state requires plastic deformation to occur principally through a reduction in wall thickness that is resisted by the crystallographic texture of the cladding. The scenario underscores the need to develop an elastic/plastic, stress/strain constitutive model for zirconium alloy cladding tubes based on data from multi-axial loading.

Displacement-controlled tensile loads from PCI are generally theorized to be the dominant loading mechanism early during an overpower transient [4][5]. This has led to many mechanical studies of cladding deformation using an expanding mandrel experiment where the displacement can be finely controlled. The resulting cladding strain can be measured through a variety of mechanical and optical means. Thus often, the goal of such studies is to find a strain-based failure criteria depending on cladding hydrogen content and temperature. A common way of achieving displacement-controlled tangential loading is through an expansion due to compression test where the displacing mandrel's radial expansion is achieved through its axial compression [6][7]. While the radial displacement can be precisely controlled in this manner, the transferred force is not multi-axial. While additional constraining loads can be added to achieve a multi-axial condition, this leads to a complicated testing setup. Additionally, such tests can also produce a bending moment in the cladding around the edge of the compressed mandrel. In an alternative testing arrangement known as "modified burst tests" (MBT), radial expansion is achieved through internal pressurization of a driver tube [8][9]. This enables the MBT to transfer a multi-axial load that is displacement controlled. Calculation of stresses in both testing arrangements requires knowledge of mandrel cladding interaction as well as a high-confidence mechanical model of the mandrel to determine the magnitude of the translated force. While these tests provide useful data to assess ductility changes, the inability to measure cladding wall stresses limits the ability of these studies to evaluate stress strain correlations. Simple internal pressure tests offer the advantage of easily determining the cladding stresses, in the axial (σ_Z), tangential (σ_θ), and radial (σ_R) directions from the internal pressure (P) using the tube internal radius (R_i) and wall thickness (t) from Equations (1), (2), and (3), based on thin wall approximation [10]. The von Mises effective stress (σ_e) under internal pressure (plane stress) is also easily deduced as shown in Equation (4) [11].

(1)

(2)

(3)

(4)

However, traditional pressure/burst tests are load controlled making determination of the ultimate tensile stress and uniform elongation limit difficult as the load is always increasing. Load controlled pressure burst tests have been performed to study the performance of Zircaloy and hydrided Zircaloy cladding tubes in this manner by Nagase and Fuketa [12][13]. These experiments clearly show the decreased in pressure capability and elongation at burst for tests with unfavorable hydride orientations. Load controlled pressures tests have also been performed to measure constant load creep properties such as work done by Lan et al [14] and Seok et al [15]. Tests by Nguyen et al incorporated a constraining biaxial tensile load and numerous instrumentations to determine the cracking behavior of coated Zircaloy claddings under varying stress biaxiality ratios at room temperature [16].

The following work is motivated by the desire to devise an internal pressure test that can mimic a displacement-controlled loading scenario and demonstrate how to apply the multi-axial stress and strain data from the test to develop an elastic/plastic constitutive model for the thin-walled structural component at prototypic temperatures.

II. Model Formulation

The coordinate system used in the elastic/plastic constitutive models below is the most convenient for thin-walled tubing. The coordinate system is Cartesian when one examines a differential element of cladding material with the first direction aligned with the tube's circumference (tangential or hoop direction), the second direction aligned with the tube's axial length, and the third direction aligned with the tube's radius. Throughout this work these directions will be referred to as the tangential (θ), axial (Z), and radial (R) directions, respectively. The tangential coordinate (θ) is a linear expression of the tube circumference or diameter and should not be confused with the common angular direction used in cylindrical coordinate systems. The models utilize the variable (σ) for the true stress and the variable (ε) for the true strain.

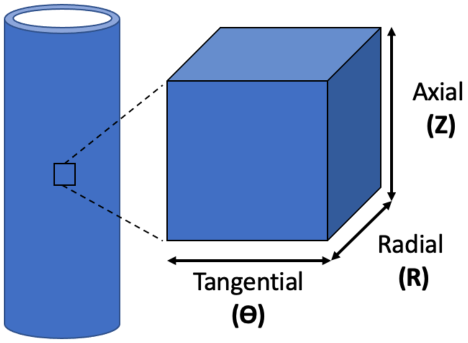

Figure 1. Coordinate System for Cladding Deformation Analysis

In the elastic regime the multi-axial constitutive law can take a generalized form of Hooke's law where the shear stresses and shear strains are equal to zero. While yielding of thin-walled zirconium alloy tubing is known to be anisotropic, the elastic behavior is treated as isotropic. The stiffness matrix (S) can be expressed in terms of a Young's modulus (E) and Poisson's ratio (ν) as shown in Equation (5).

(5)

Strictly speaking, the strain vector (ε) in Equation (5) is an elastic strain vector. In the plastic regime, the plastic strain components must be subtracted from the total strains so that only the elastic components of strain are multiplied by the stiffness matrix. Determination of the plastic strain vector () requires the formulation of a multi-axial anisotropic yield function and an associated hardening law. The direction of the plastic strain vector comes from application of the plastic flow rule by taking the gradient of the yield function, and the magnitude of the plastic strain vector comes from the hardening law. The yield function will take a simplified form of Hill's anisotropic yield criterion neglecting the shear components, as shown in Equation (6) [17]. So that the Hill coefficients (F, G, and H) are purely directional in nature, the function is normalized by a value of $(\sigma_{e,p})^2$. The coefficient ($\sigma_{e,p}$), called the flow stress, is equal to the von Mises effective stress after yielding under an internal pressure loading. A simple power law hardening relationship is assumed, which is valid only for monotonically increasing loads and is shown in Equation (7). The equation applies the consistency condition for plastic flow and updates the flow stress ($\sigma_{e,p}$) from the yield stress ($\sigma_{e,p,yield}$) by a hardening coefficient (K) and the equivalent plastic strain () raised to a strain exponent (n).

(6)

(7)

Three independent equations are needed to solve for the Hill coefficients. Solutions for the Hill coefficients are traditionally found by conducting uniaxial tensile tests in each of the principal orthogonal directions (θ, Z, and R). However, this presents experimental challenges with thin-walled tubing and conflicts with the aim of evaluating material performance under multi-axial loading conditions. Internal pressurization provides an easily quantifiable multi-axial stress state for thin-walled tubing making this loading scenario an ideal initial selection. Substituting Equations (2) and (3) into Equation (6) allows one to derive Equation (8).

(8)

A second equation can be derived from the internal pressure test through the application of the plastic flow rule which states that the direction of the plastic strains must be normal to the yield surface. Taking the gradient of Equation (6) and then again substituting Equations (2) and (3) allows one to equate the Hill coefficients to defined plastic strain ratios under an internal pressure load. These formulations are shown in Equations (9), (10), and (11). Note that these relationships are only valid under capped internal pressure loading and different correlations would need to be developed under uniaxial loading or with different multi-axial stress ratios.

(9)

(10)

(11)

Equations (9), (10), and (11) are not independent thus requiring an additional equation, and the loading scenario, to fully develop the Hill coefficients. A uniaxial full-tube tension test in the axial (Z) direction makes an ideal complement to the internal pressure test as it is similarly straightforward to conduct and provides the necessary independent loading scenario. Under a uniaxial load in the axial (Z) direction, Equation (6) can be reduced as the principal stresses in the tangential (θ) and radial (R) direction are zero. This leads to a third independent equation (12) used to solve for the Hill coefficients.

(12)

III. Test Procedure

Both full-tube axial tension tests and internal pressure tests are conducted to meet the data needs identified in the above model formulation. In both test configurations the test samples are loaded inside a custom box furnace capable of elevating the test sample temperature. The box furnace also provides the containment and safety function for the pressure tests. An argon purge line is connected to the furnace to limit sample oxidation during high-temperature testing. Epsilon Model 7675-025M and Model 7642-010M-025M high-temperature extensometers are used to monitor the tangential (θ) and axial (Z) expansion of the cladding tube during the tests. The full-tube axial tension tests are conducted using a standard Instron model 5967 universal testing machine.

For the internal pressure tests a Maxpro MTIG20-30-75-2 booster pump is used to elevate the pressure of an argon gas source up to 135 MPa. A Tescom 26-2000 pressure-reducing regulator, which is pneumatically controlled by a Tescom ER5000 controller, reduces the pressure in a downstream static pressure line to a desired set point. Pressure is monitored in an active feedback loop via a Tescom 2168 pressure transducer located behind the pressure-reducing regulator. The Tescom 26-2000 has a vent port so that pressure in the static line can be reduced if the pressure set point is lowered. Test samples are connected to the static pressure line using medium pressure Swagelok fittings behind a bulkhead. A dead leg of medium pressure tubing is connected to the other end of the test sample and capped. The dead leg of the medium pressure tubing is axially unconstrained. An additional pressure transducer is located immediately below the bulkhead to obtain the most accurate internal pressure measurement in the sample. Between the two pressure transducers is a fast-acting nominally open Remarco solenoid valve programmed to close upon a significant pressure drop such as would occur if the test sample ruptured, limiting the amount of high-pressure compressed gas being expelled through the ruptured test sample. Figure 1 shows a schematic of the testing apparatus. A pseudo displacement-controlled test is achieved by programming the tangential (θ) extensometer into a proportional integral derivative feedback loop with the system pressure setpoint, using a Labview data acquisition system. Testing was terminated upon a 1 MPa drop in the pressure setpoint from its maximum value indicating that maximum uniform elongation had been achieved.

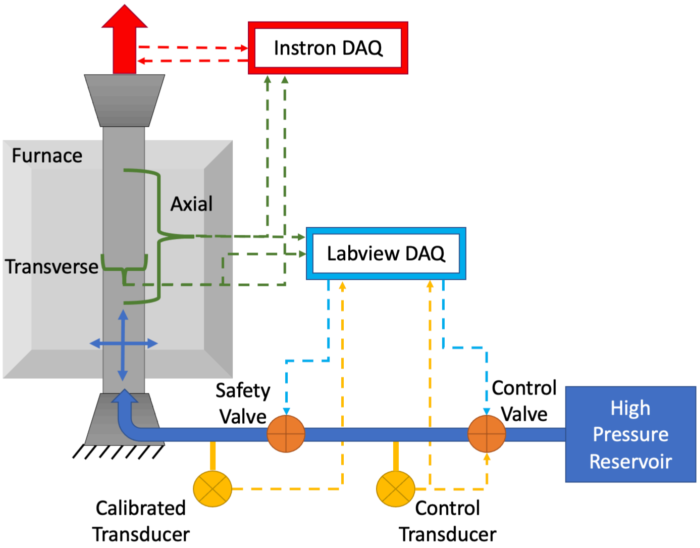

Figure 2. Cladding axial tension and pressure testing apparatus.

Zircaloy-4 cladding tubes with a nominal outer diameter of 9.5 mm and a wall thickness of 0.57 mm cut into 150 mm lengths are used in the present study. These tubes were commercially procured and conform to ASTM B353-12 [18]. Figure 32 shows a test sample with the tangential (θ) and axial (Z) extensometers connected to the testing apparatus. Tests are conducted at room temperature (~22°C), 150°C, 275°C, 400°C, and 525°C. The samples are heated for ~3 hours to reach the isothermal target temperature. The cladding was deformed at a programmed strain rate of 0.1% per minute. The programmed strain rate corresponds to the tangential (θ) strain in the pressure test and the axial (Z) strain in the full-tube tension test. The loading rate either from internal pressurization or axial loading is not constant as these are strain controlled tests and the loading rate varies to achieve a programmed strain rate.

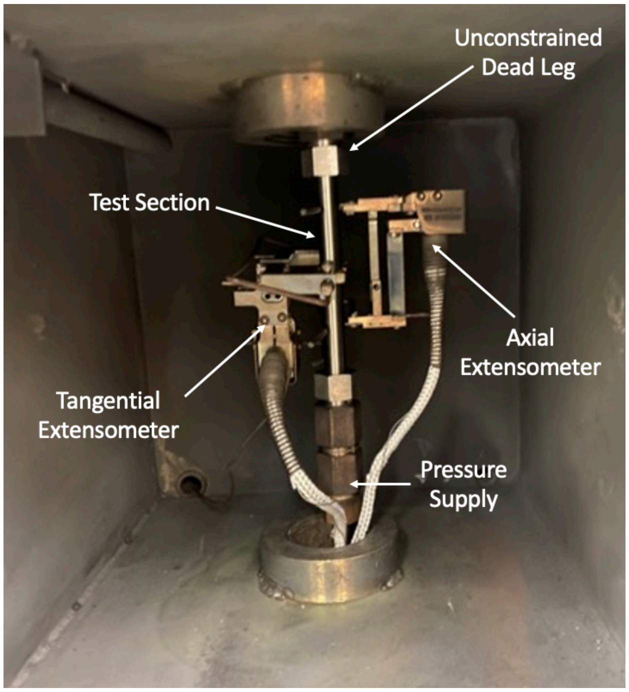

Figure 3. Zircaloy-4 cladding tube in pressure test apparatus

IV. Analysis Procedure

The first step in the data analysis is the determination of the yielding point. The yield point in both tests is determined by an offset line. The goal of the yield point determination is to determine when plastic deformation begins, and plastic strains begin to accumulate. For the pressure test, the slope of the offset line is equal to the rate of change of pressure in the elastic region. For the full-tube tension test the slope of the offset line is equal to the rate of change of the axial stress in the elastic region. The high-confidence elastic region used to develop the loading rates is determined for each temperature based on observed linearity in the data. The offset time is equal to the programmed strain rate divided by a defined strain offset of 0.02%. The yield point is the first point in the test at which the load crosses below the offset line. While it is conventional to use a 0.2% offset line to determine the yield strength, it was found that a significant deviation from linearity of the stress/strain response was observed between 0.02%

and 0.2%. Thus, it was chosen to use a more stringent yield condition of 0.02% in this study. For the full-tube tension test Young's modulus (E) and Poisson's ratio (ν) can be found from an expansion and solution to equation (5) which are shown below in equations (13) and (14). In these equations the variable (s) used for the engineering stress and the variable (e) used for the engineering strain. It is common engineering practice to use the measured engineering values to derive elastic constants and differences between engineering stress/strain and true stress/strain values are generally negligible in the elastic region.

(13)

(14)

During the full-tube tension tests the fittings often failed after approximately 2% axial (Z) strain limiting the usefulness of these tests beyond the determination of the elastic constants and the yield stress. However, enough plastic deformation occurred to develop the plastic strain ratios. *Figure 4* shows a plot of full-tube tension test data and the derived mechanical properties as well as the α strain ratio (change in engineering hoop plastic strain over change in engineering axial plastic strain) for the axial tension loading scenario.

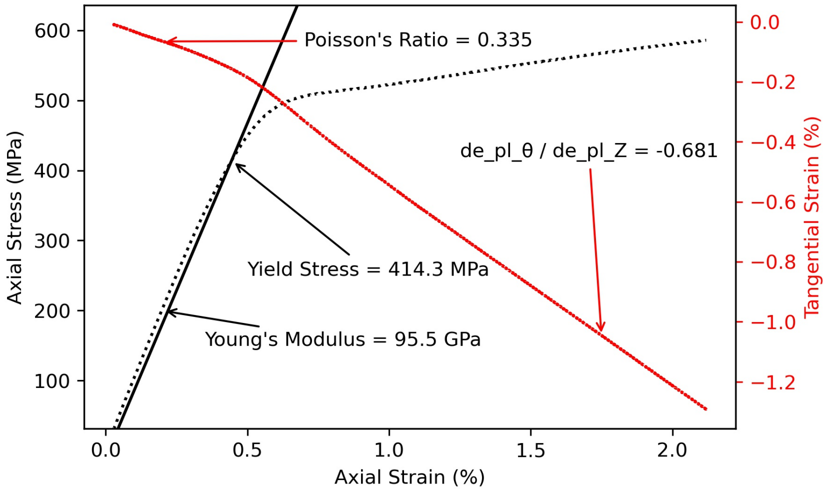

Figure 4. Stress strain data from a full tube tension test at room temperature

Young's modulus (E) and Poisson's ratio (ν) are determined from pressure test data using an expansion of the multi-axial formulation of Hooke's law in Equation (5). These formulations are shown in Equations (15) and (16). *Figure 5* shows a plot of internal pressure test data and the derived mechanical properties.

(15)

(16)

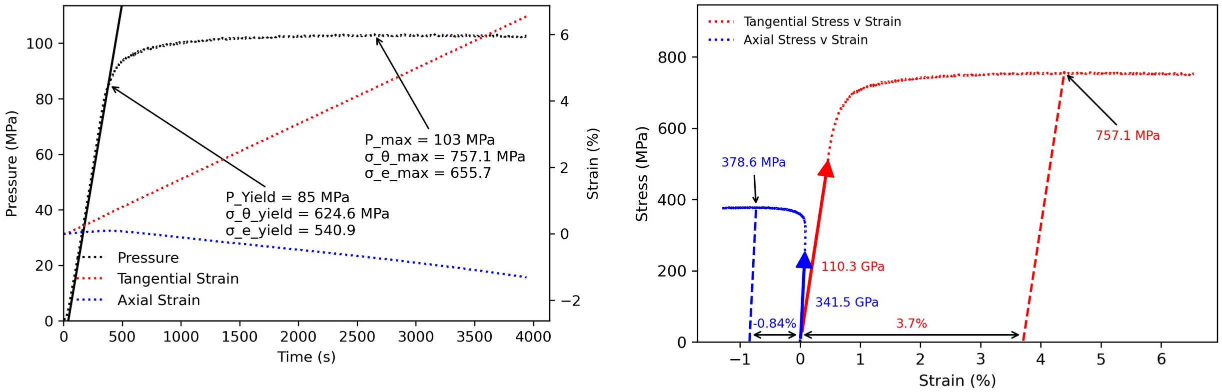

Figure 5. Stress strain data from an internal pressure test at room temperature; Young's Modulus was equal to 90 GPa and Poisson's Ratio was equal to 0.368 in this test.

A. Strain Decomposition

Determination of the true plastic strain ratios in the internal pressure test requires a separation of the measured strains into their elastic and plastic components after yielding. The elastic components of strain can be determined from the derived elastic constants and Equation (5). Tangential (θ) and axial (Z) components of true plastic strain can then be determined by subtracting the elastic components from their measured engineering values and applying natural logarithms as shown in equation (17).

(17)

Determination of the radial (R) component of plastic strain requires application of the incompressibility criterion for plastic flow, which states that the true plastic strain rates along three orthogonal directions must equal zero. Integrating the incompressibility criteria for the measured data set from the yield point (assume plastic strain at the onset of yielding is equal to zero) allows one to derive Equation (18). Figure 6 shows the full decomposition of strains and the calculated strain ratios from an internal pressure test at room temperature. The negative axial (Z) plastic strain (dashed blue line) confirms the expected anisotropic nature of the tubing as the volume conservation during tangential expansion of the tubing is accomplished not only by wall thinning but also by axial shrinkage.

(18)

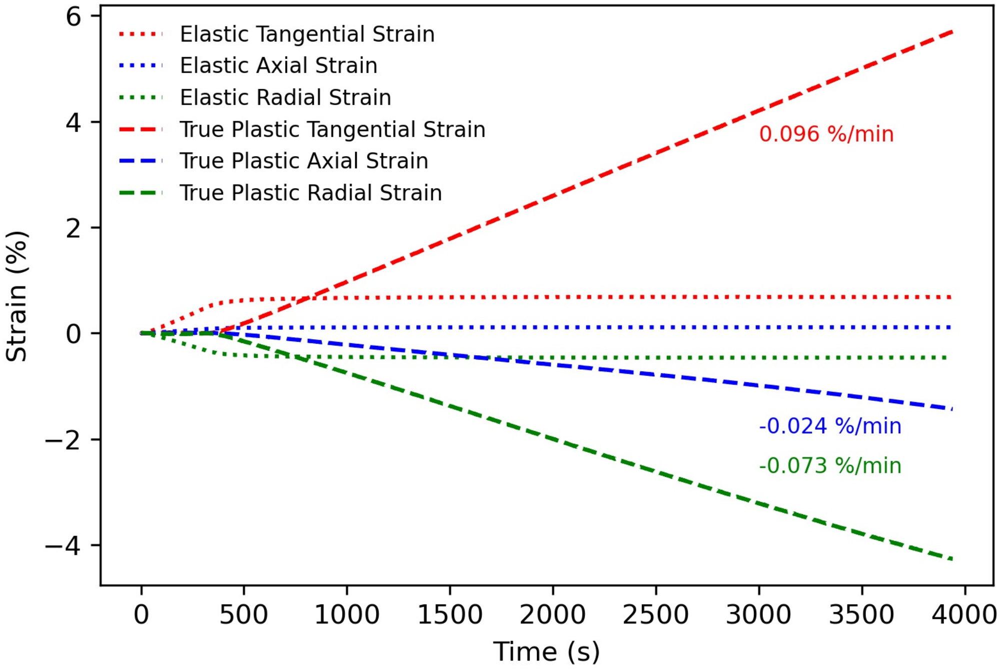

Figure 6. Decomposition of elastic and plastic strain components in a room temperature pressure test

B. Power Law Hardening

It is assumed that during hardening the yield surface expands isotropically and that the degree of anisotropy does not change during hardening. This assumption is valid for monotonically increasing tensile loads with finite plastic strains. Under this assumption, a power law hardening model can be fitted to the data by relating an equivalent plastic strain to the von Mises effective true stress. The equivalent plastic strain can be determined from the plastic strain rate components derived above and then using a strain energy balance. The derived formulation is shown in Equation 19. Then, using the engineering tangential (θ) strain and engineering radial (R) strain to determine the true dimensions of the deformed cladding tube, the true axial (Z) stress is determined in Equation 20. The engineering radial strain used in Equation (20) is determined by re-arranging Equation (17) to solve for the total engineering strain for a given true plastic strain and elastic strain. True tangential (θ) stress can then be determined from Equation (2) and the true von Mises stress from Equation (4).

(19)

(20)

The hardening coefficient (*K*) and the strain exponent (*n*) are determined by taking natural logarithms of Equation (7) and performing a linear regression where the slope of the regression line is equal to the strain exponent (*n*) and the intercept of the regression line is equal to the natural logarithm of the hardening coefficient (*K*). Figure 7 shows a comparison between the data and the derived hardening model. The blue line plots the effective mises true stress after yielding against the equivalent plastic strain calculated in equation (19). The orange line plots the relationship using the derived K and n for an internal pressure test at room temperature. The fit is adequate but not ideal.

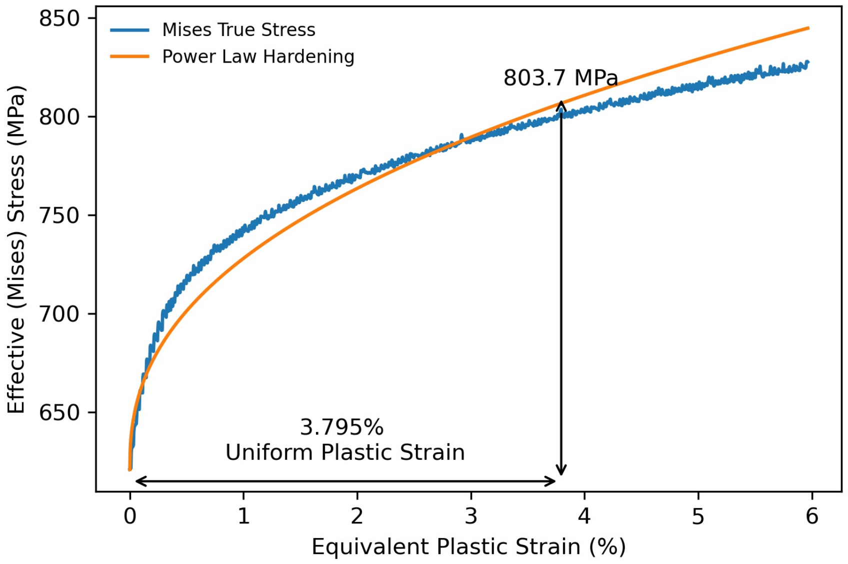

Figure 7. Hardening behavior from an internal pressure test at room temperature, K was equal to 716 MPa and n was equal to 0.413 in this test.

V. Results

Thirteen pressure tests and five full-tube tension tests were conducted according to the procedures described in section III with results shown in Table 1 and Table 2. Of the five full tube tension tests three were conducted at room temperature and two were conducted at 400 °C. Of the 13 pressure tests four were done at room temperature, two at 150 °C, three at 275 °C, three at 400 °C and one test at 525 °C. The tangential (θ) stress and effective stress at yielding are both reported for the internal pressure tests. For the single pressure test at 525 °C, the cladding displayed a yield drop softening behavior in which most of the plastic flow occurred below the maximum load making calculation of the plasticity variables difficult using the methods described above. It is hypothesized that at this temperature and above visco-plastic effects begin to dominate the deformation.

Results are generally consistent at a given temperature with variability between the elastic and strength properties generally varying by less than 5%. The greatest variability is seen in the hardening data with as much as 16% variability in the hardening coefficient (K) and as much as 11% variability in the strain exponent (n). The fit of the power law hardening model to the data is acceptable (R^2 >95%) although the fit regularly underestimates yield and overestimates the hardening behavior, as seen in Figure *7*. It has been suggested by other authors that there is an inherent randomness in the onset of plastic instabilities in unirradiated zirconium alloys [19][20]. This is explained by the anisotropic microstructure of the cladding tubes. The geometrically favored deformation system of the cladding's microstructure resists microplasticity until the critically resolved shear stress (CRSS) of a system is achieved, at which point plastic deformation may occur on all similar systems. The sudden activation of many similar slip systems will display a sharper yield shoulder than observed in more isotropic materials as well which can also be seen in Figure *7*. More refined hardening models may be needed to account for this behavior and will be explored as part of future work.

Yield stress and ultimate tensile stress consistently decrease with temperature. Other mechanical property changes are most notable between 275 °C and 400 °C. Over this temperature range Young's modulus decreases from an average value of 84.5 GPa to an average value of 68.4 GPa. This is consistent with the expected 5% drop per 100 °C expected in HCP metals of the IV-B row in the periodic table [21]. The hardening coefficient likewise decreases from an average value of 655.3 MPa to 426 MPa. The decrease in the hardening coefficient with temperature is consistent with other correlations [20]. The ductility also begins to dramatically drop off in this temperature region with engineering uniform elongation in the tangential (θ) direction decreasing from 3.8% to 1.9%. For internal pressure loadings the uniform elongation in the tangential (θ) direction is very close to the true equivalent plastic strain, which is convenient for interpreting the results from these tests. However, care should be taken as this is not generically true. Under other stress ratios significantly higher contributions to the equivalent plastic strain can come from other strain components resulting in higher plastic strains (and thus higher wall stresses) at a similar tangential (θ) elongation.

Young's modulus, Poisson's ratio, yield stress, and ultimate tensile stress from the developed data set were compared with a variety of literature sources. Plots are shown in Figure 8, Figure 9, Figure 10, and Figure 11. When shown in these figures, data from axial tension tests are plotted as squares, data from ring tension tests are plotted as triangles, and data are plotted as dots when only effective stresses are listed with no additional information on testing direction. For Young's modulus the data from both internal pressure and axial tension tests is in good agreement with literature from a large variety of sources [19][20][22][23][24][25][26][27][28][29][30][31][32][33][34][35], up to 400 °C. At 525 °C creep loci are likely being encountered very early in the internal pressure test and biasing the measurement of Young's modulus low. The data for Poisson's ratio is likewise in good agreement with a variety of sources at room temperature [19][23][24][25][33][35] and closely tracks data from Schwenk [36] up to 400 °C. Data is notably lower than values reported by Scott [31]. Few sources provide measured data points above 400 °C for comparison.

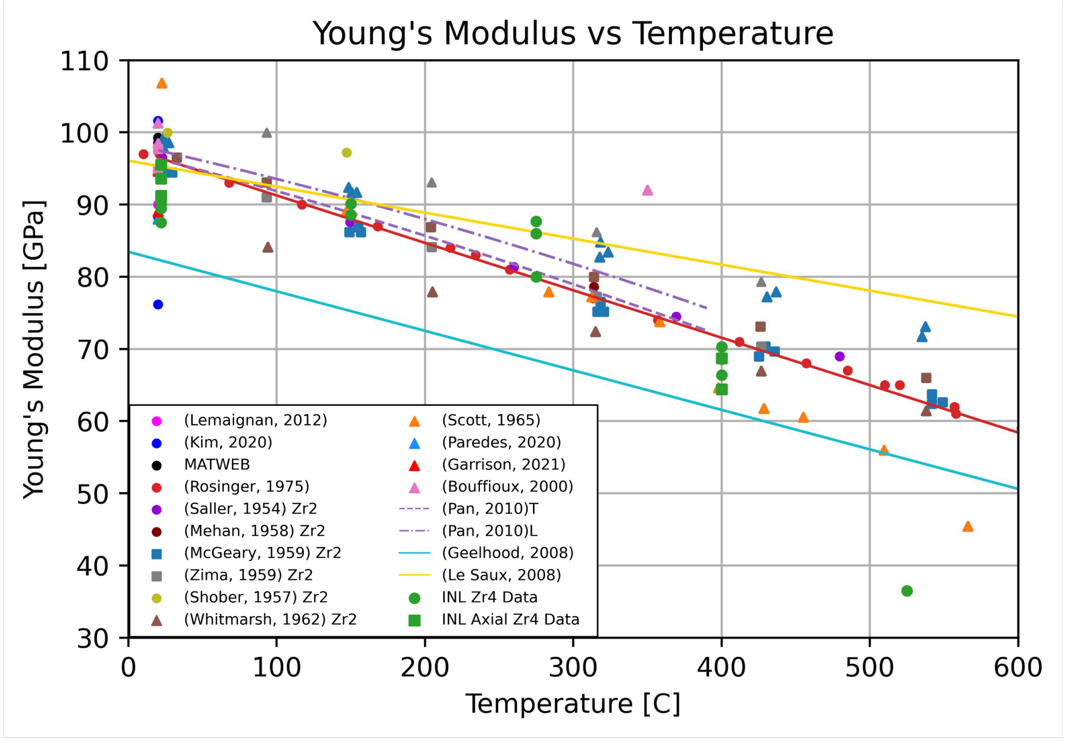

Figure 8. Comparison of Young's Modulus Data with Literature

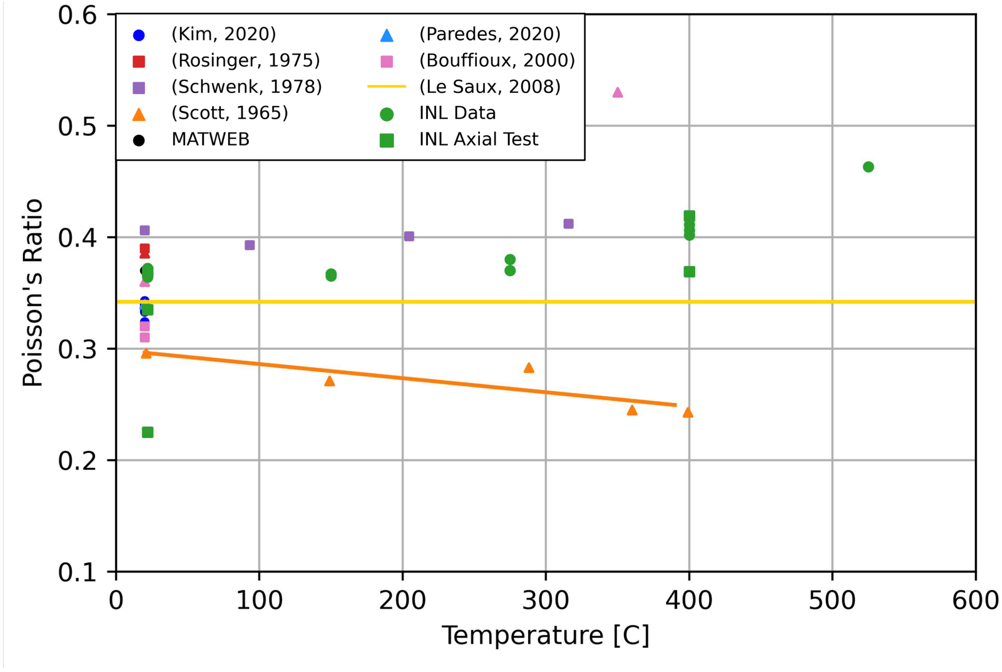

Figure 9. Comparison of Poisson's Ratio Data with Literature

There is much greater variability among literature sources regarding measured yield stresses and ultimate tensile stresses. These strength values are much more sensitive to material processing parameters, such as the degree of cold work and final heat treatment as well as differing among the specific zirconium alloy being tested. With respect to yield stress, the values derived in this study fall within the wide range of reported values from room temperature studies [19][20][24][37][38][39][40][41][42][43]. They also track well with data from Huang [44] and Tung [45] up to 400 °C. The ultimate tensile stress (UTS) values derived from this study tended to be generally higher than literature. It is unclear from many of the references if engineering or true stresses were used for the UTS which may account for some of the differences. Bouffioux et al. [33] explicitly use the true stress value corresponding to their UTS data which best matches the data in this study. Mozzani et al. [41] explicitly use engineering values for the yield stress and UTS data which agree well with other sources transposed by a constant stress factor from the true stress data at significant plastic strain.

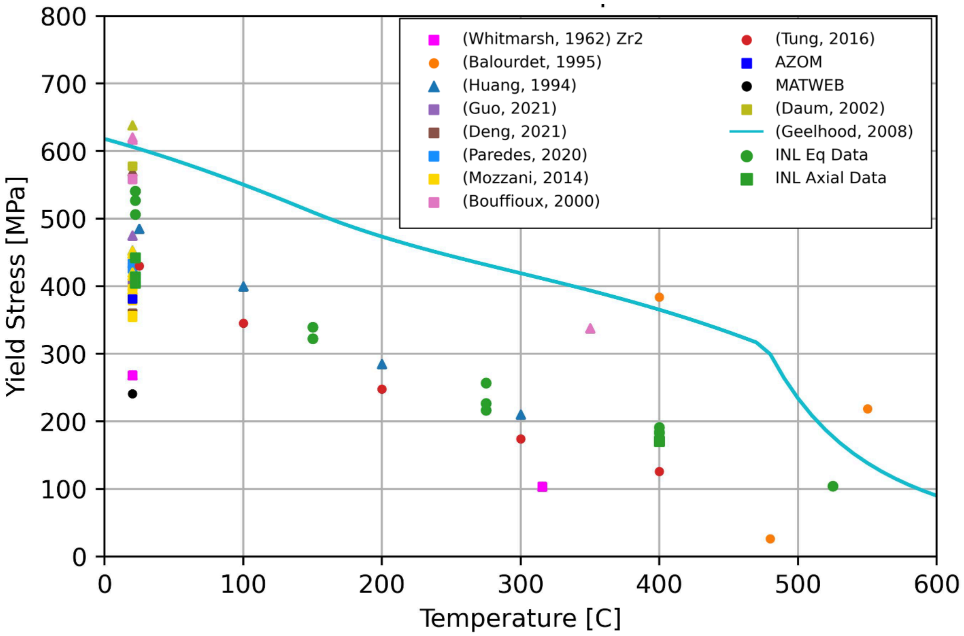

Figure 10. Comparison of Yield Stress Data with Literature

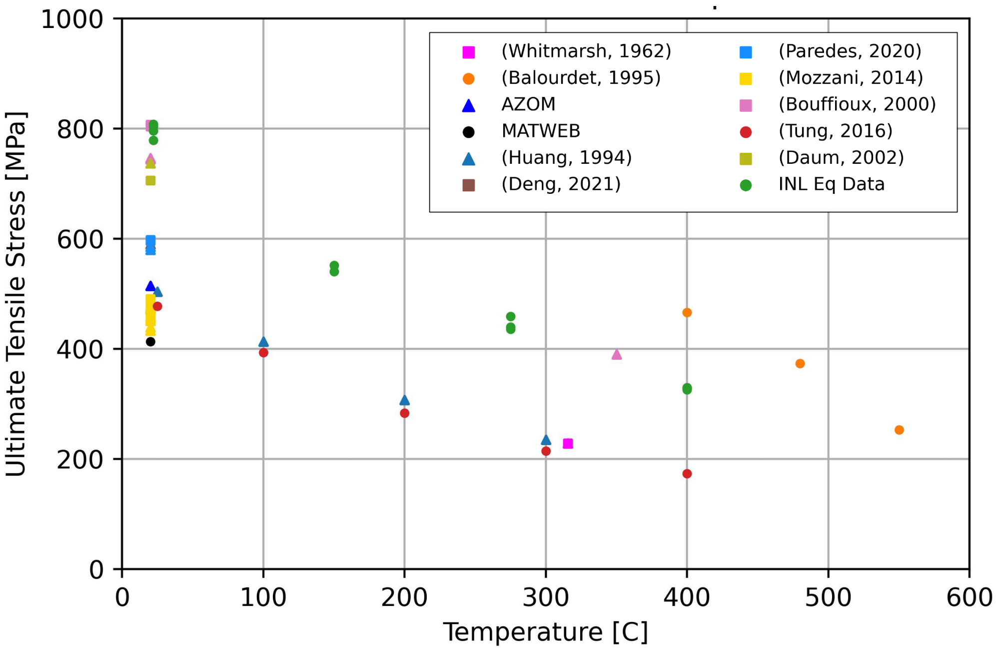

Figure 11. Comparison of Ultimate Tensile Stress Data with Literature

Table 1. Results from Pressure Tests

Stress at Yielding		Elastic Properties		Plastic Strain Ratios			Hardening Constants		Ductility Measures		Ultimate True Stress
$\sigma_{\theta,yield}$ (MPa)	$\sigma_{e,p,yield}$ (MPa)	E (GPa)	v	α	β	γ	K (MPa)	n	θ-UE (%)	Max ε^p (%)	Max σ_e (Mpa)
Room Temperature (~20 °C)											
624.5	540.8	89.5	0.366	-3.708	-1.369	0.369	559.2	0.392	4.58	4.631	795.5
608.5	526.9	87.5	0.372	-4.161	-1.316	0.316	758.7	0.412	4.54	4.661	808
624.6	540.9	90	0.368	-4.062	-1.327	0.327	716.7	0.413	3.7	3.795	803.7
584.4	506.1	90.4	0.364	-3.67	-1.375	0.375	595	0.373	5.05	5.102	778.6
150 °C											
372.4	322.5	90.1	0.365	-2.478	-1.677	0.677	579.6	0.386	4.4	4.331	540.3
391.9	339.4	88.6	0.367	-2.649	-1.607	0.607	589.4	0.383	2.79	2.788	551.1
275 °C											
261.8	226.8	87.7	0.37	-3.067	-1.484	0.484	736.5	0.422	4.15	4.152	435.2
250.2	216.7	80	0.38	-3.256	-1.443	0.443	691.2	0.389	3.95	3.994	439.4
296.7	256.9	86	0.37	-3.189	-1.457	0.457	538.2	0.358	3.4	3.352	458.9
400 °C											
210.9	182.7	66.4	0.411	-6.452	-1.183	0.183	428.1	0.355	1.96	2.139	328.3
213.1	184.5	68.6	0.402	-6.577	-1.179	0.179	387.5	0.322	1.89	2.057	329.7
220.3	190.8	70.3	0.406	-6.752	-1.174	0.174	463.1	0.404	1.91	2.058	325.3
525 °C											
120.5	104	36.5	0.463								

*θ-UE – Engineering Tangential Strain ‘Elongation’ Prior to Load Drop

**ε^p – True Equivalent Plastic Strain Prior to Load Drop

Table 2. Results from Full Tube Tension Tests

$\sigma_{Z,yield}$ (MPa)	E (GPa)	v	α
Room Temperature (~20 °C)			
442.1	91.2	0.369	-0.673
414.3	95.5	0.335	-0.681
404.5	93.6	0.225	-0.586
400 °C			
171.1	64.4	0.369	-0.673
170.2	68.7	0.419	-0.718

VI. Derivation of Hill Coefficients & Yield Loci

The developed data set allow for the simultaneous solutions to Equations (8), (9), and (12) to calculate Hill anisotropic yield coefficients at room temperature and 400 °C. Figure 12 shows these coefficients along with the corresponding yield loci. The effect of the power law hardening can also be seen by the dashed blue line. For reference, the von Mises yield loci that would be calculated from a uniaxial axial tension test (green) and a ring tension test (magenta) are also shown for comparison. Data from previously conducted ring tension tests by the author is used to develop the yield loci in the figure for the tangential (θ) loading condition [46]. The derived curves show how applying data from uniaxial tests in either the tangential (θ) or axial (Z) direction would lead to an under calculation of tangential (θ) stresses and the importance of conducting multi-axial testing. Even if one does not fully develop a Hill yield criterion, using a von Mises criterion based on the effective yield stress in an internal pressure test provides a much more accurate calculation of wall stresses during multi-axial yielding as shown in the red curve.

The model predicts a maximum tangential (θ) stress when the axial (Z) to tangential (θ) stress ratio is 0.64. The derived Hill yield loci predicts a uniaxial tangential (θ) yield stress of 452.3 MPa. This closely matches the uniaxial data from ring tension testing data, which reported yield stresses of ~470 MPa [46]. The Hill yield model can be further cross validated by comparing the calculated plastic strain ratios for the axial tube tension test with those predicted by the model. Application of the plastic flow rule to Equation (6) and setting the radial and tangential stresses equal to zero results in Equation (21). Taking the derived room-temperature Hill coefficients for H and F result in a plastic strain ratio of -0.639, which is very close to the average of the measured values in the axial tension tests at room temperature of -0.647.

(21)

These numerous cross validations show that the internal pressure test is most useful in development of mechanical property data, and that it can be used to simulate PCI loading scenarios. At 400 °C, the tubing anisotropy is significantly reduced, and the Hill yield values all approach 0.5. The 400 °C Hill yield and von Mises yield loci for internal pressure and axial tensile data are shown in Figure 13. While axial tensile tests were not conducted at 150 °C or 275 °C, the plastic strain ratios developed from the internal pressure tests indicate that anisotropy is even higher at these intermediate temperatures than at room temperature. It is likely that the high flow stresses that develop at room temperature activate more twinning slip systems in the radially aligned basal poles. At 400 °C, slip system CRSS become more isotropic, and diffusion activated slip systems further allow for more deformation in the radial direction. However, stresses at intermediate temperatures are too low to activate twinning based systems and the temperatures too low to create any predominating diffusion processes [47]. It is theorized that at these intermediate temperatures and stresses that deformation is limited to dislocation-based slip on prismatic <a> systems and thus mechanical anisotropy due to grain texture is highest in these domains. Validating this hypothesis will be the subject of future work.

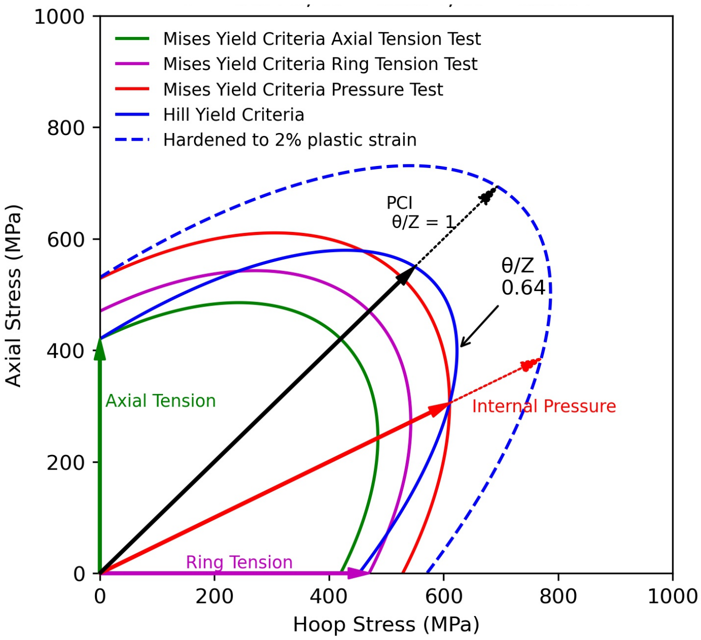

Figure 12. Yield Loci from Hill Yielding Criteria at Room Temperature; F=0.571, G=0.354, H=1.012

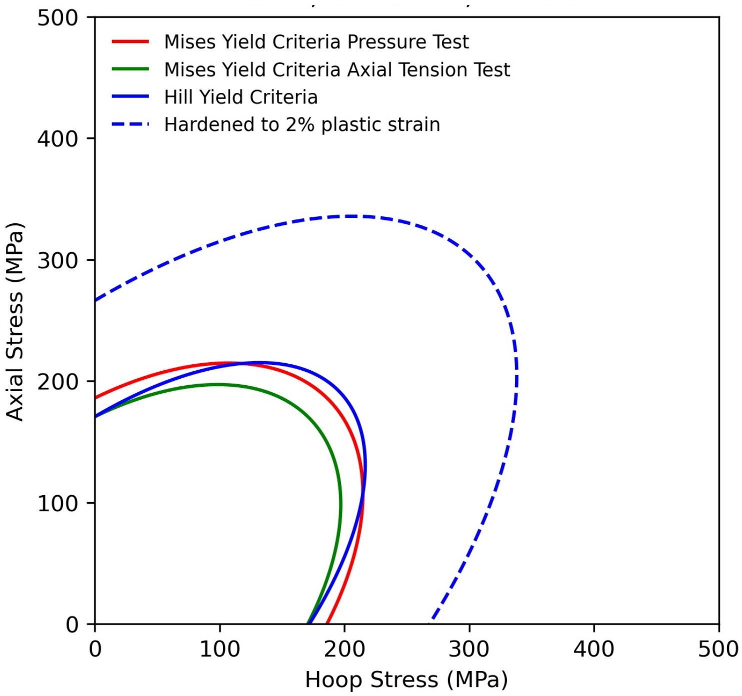

Figure 13. Yield Loci from Hill Yielding Criteria at 400 C; F=0.47, G=0.453, H=0.718

The results of this study confirm that fresh, unirradiated and non-corroded (no hydrogen pickup) cladding has sufficient ductility to accommodate displacement-controlled loadings from an expanding fuel pellet. These results also indicate that if the deformation occurs at low temperature, such as in a cold zero-power transient, significant wall stresses can be generated for even modest tangential (θ) displacements. These stresses will likely be even higher if one considers strain rate [39] and irradiation hardening effects [48]. In claddings with a significant hydride flaw, these stresses may be high enough to initiate a cleavage-style crack [49]. As the cladding heats up, the stresses are relieved; however, if a flaw has already been initiated from a low-temperature stress fracture in a hydrided region, the limited amount of hardening that occurs past ~2% plastic strain in the bulk metal limits the ability of the crack to arrest. Even at low-engineering strains from PCI, local ductility can be quickly exhausted in these cases. This leads to the characteristic fracture surface seen in many fractured cladding tubes from overpower transient tests, which have a Mode I brittle crack in a heavily hydrided region, followed by a mixed Mode I/Mode II ductile crack propagating from the tip of the brittle flaw through the cladding thickness, ultimately resulting in failure [50].

VII. Conclusions

It is concluded that the internal pressure test is capable of simulating displacement-controlled loadings and can generate a large set of useful mechanical property data on thin-walled zirconium alloy tubing up to 400 °C. When combined with full-tube axial tensile tests, the data from the internal pressure test can be used to derive Hill yield coefficients to develop a multi-axial elastic/plastic constitutive model of thin-walled tubing. The derived mechanical properties from the multi-axial loading experiments generally have low variability between tests and compare well with data derived from many literature sources. This validates the use of the test method to develop reliable data with a few tests. Texture induced mechanical anisotropy is identified at room temperature and appears to be minimized at high temperatures, in this case at 400 °C. However, the study provides some evidence that the mechanical anisotropy may be at a maximum around 150 °C or between 150 °C and 275 °C. The importance of conducting multi-axial loading experiments is emphasized as the developed yield loci showed that notably higher yield stresses are seen for thin-walled zirconium alloy metals under multi-axial loading than under uniaxial loading in either the axial (Z) or tangential (θ) directions. The developed yield loci are cross validated by comparing the plastic strain ratios from the full-tube tension tests and by comparing the predicted yield stress in the tangential di-rection with measured values from ring tension tests in a previous study.

VIII. Acknowledgements

This work was supported through the U.S. Department of Energy Advanced Fuels Campaign under DOE Idaho Operations Office Contract DE-AC07-05ID14517. Accordingly, the U.S. Government retains and the publisher, by accepting the article for publication, acknowledges that the U.S. Government retains a nonexclusive, paid-up, irrevocable, world-wide license to publish or reproduce the published form of this manuscript, or allow others to do so, for U.S. Government purposes.

IX. Declaration of Interest

This information was prepared as an account of work sponsored by an agency of the U.S. Government. Neither the U.S. Government nor any agency thereof, nor any of their employees, makes any warranty, express or implied, or assumes any legal liability or responsibility for the accuracy, completeness, or usefulness of any information, apparatus, product, or process disclosed, or represents that its use would not infringe privately owned rights. References herein to any specific commercial product, process, or service by trade name, trademark, manufacturer, or otherwise, does not necessarily constitute or imply its endorsement, recommendation, or favoring by the U.S. Government or any agency thereof. The views and opinions of authors expressed herein do not necessarily state or reflect those of the U.S. Government or any agency thereof.

REFERENCES

1. E. Tenckhoff, “Review of Deformation Mechanisms, Texture, and Mechanical Anisotropy in Zirconium and Zirconium Base Alloys,” ASTM Int., Vol. 2, (2005).

2. S. Banerjee “Nuclear Applications: Zirconium Alloys” Encyclopedia of Materials: Science and Technology, (2001).

3. M. Suzuki, H. Saitou, T. Fuketa “Analysis on pellet-clad mechanical interaction process of high burnup PWR fuel rods by RANNS code in reactivity-initiated accident conditions” Nuclear Technology, Vol. 155, (2006)

4. Nuclear Energy Agency, Nuclear Fuel Behavior Under Reactivity-initiated Accident Conditions State of the Art Report, NEA No. 6847, (2010).

5. Fuketa T. “Transient Response of LWR Fuels (RIA)” Comprehensive Nuclear Materials 2.22, (2012).

6. Hellouin de Menibus A., Auzoux Q., Monagabure P., Macdonald V., Le Jolu T., Besson J., Crepin J., “Fracture of Zircaloy-4 cladding tubes with or without hydride blisters in uniaxial to plane strain conditions with standard and optimized expansion due to compression tests” Materials Science and Engineering, Vol 604, (2014).

7. Shinozaki T., Udagawa Y., Mihara T., Sugiyama T., Amaya M., “Improved-EDC tests on the Zircaloy-4 cladding tube with an outer surface pre-crack” Journal of Nuclear Science and Technology, Vol 53, (2016).

8. Yueh K., Karlsson J., Stjarnsater J., Schirire D., Ledergerber G., Munoz-reja C., Hallstadius L., “Fuel cladding behavior under rapid loading conditions” Journal of Nuclear Materials, Vol. 469, (2016).

9. Yueh K., “Applicability of modified burst test data to reactivity initiated accident,” Journal of Nuclear Materials, Vol 488, (2017).

10. Engineering ToolBox, (2005). Stress in Thin-Walled Cylinders or Tubes. [online] Available at: https://www.engineeringtoolbox.com/stress-thin-walled-tube-d_948.html [Accessed 1 Aug. 2022]

11. Mises, R. v.. "Mechanik der festen Körper im plastisch- deformablen Zustand." Nachrichten von der Gesellschaft der Wissenschaften zu Göttingen, Mathematisch-Physikalische Klasse, (1913): 582-592. http://eudml.org/doc/58894

12. Nagase, F., Fuketa, T., “Influence of Hydride Re-orientation on BWR Cladding Rupture under Accidental Conditions” *Journal of Nuclear Science and Technology* Vol 41 No 12 (2004)

13. Nagase, F., Fuketa, T., “Investigation of Hydride Rim Effect on Failure of Zircaloy-4 Cladding with Tube Burst Test” *Journal of Nuclear Science and Technology* Vol 42 No 1 (2005)

14. Lan, K-C., Chuang, C-P., Tung, H-M., Mo, K., Miao, Y., Liu, X., Lee, H., Park, J-S., Almer, J., Stubbins, J.F., “A study of the texture stability and the biaxial creep behavior of as-hydrided CWSR Zircaloy-4 cladding at the effective stresses from 55 MPa to 65 MPa and temperature from 300 °C to 400 °C” *Journal of Nuclear Materials* Vol. 564 (2022)

15. Seok, C-S., Bae, B-K., Koo, J-M., Murty, K.L., “The properties of the ring and burst creep of ZIRLO cladding” *Engineering Failure and Analysis* Vol 13 (2006)

16. Nguyen, D.V., Le Saux, M., Felebart, L., Brachet, J-C., Bonthonneau, J-C., Courcelle, A., Guillou, R., Rouesne, E., Urvoy, S., “Mechanical behavior of a chromium coating on a zirconium alloy substrate at room temperature” *Journal of Nuclear Materials* Vol 558 (2022)

17. Hill, R. “A theory of the yielding and plastic flow of anisotropic metals” *Proc R. Soc. Lond. A,* Vol. 193, (1948) http://doi.org/10/1098/rspa.1948.0045

18. *Standard Specification of Wrought Zirconium and Zirconium Alloy Seamless and Welded Tubes for Nuclar Service (Ecpet Nuclear Fuel Cladding)* ASTM B353-12(2022)e1

19. Paredes, M., and Wierzbicki, T. “On mechanical response of Zircaloy-4 under a wider range of stress states: From uniaxial tension to uniaxial compression.” International Journal of Solids and Structures, Vol 206, (2020).

20. Geelhood, K. J., Beyer, C. E., and Luscher, W. G. *Stress/Strain Correlation for Zircaloy*. PNNL-17700. (2008).

21. Fisher E.S., Renken C.J. “Single-Crystal Elastic Moduli and the hcp -> bcc Transformation in Ti Zr and Hf” *Physical Review* Vol 135 (1964)

22. Lemaignan, C. “Zirconium alloys: Properties and characteristics,” Comprehensive Nuclear Materials (2012).

23. Kim, H., Lee, Y., Kim, I., Kim, H., and Kim, D. “On the method to obtain the elastic properties using a pressurized thin tube,” Engineering Failure Analysis, (2020).

24. MatWeb. Zircaloy-4 Zirconium Alloy. https://www.matweb.com/search/DataSheet.aspx?MatGUID=e36a9590eb5945de94d89a35097b7faa, (2022).

25. Rosinger, H., Ritchie, I., and Shillinglaw, A. “Young’s Modulus of Crystal Bar Zirconium and Zirconium Alloys [Zircaloy-2, Zircaloy-4, Zirconium-2.5wt% Niobium] to 1000K.” Whitesheil Nuclear Research Establishment, (1975).

26. Saller, H. A., Dickerson, R. F., and Foster, E. L. Induction-Melted Zirconium and Zirconium Alloys. BMI-908, (1954).

27. Mehan, R. L. Modulus of Elasticity of Zircaloy-2 Between Room Temperature and 1000°F. KAPL-M-RLM-16, (1958).

28. McGeary, R. K., and Lustman, B. “Preferred Orientation in Zirconium,” Trans. AIMME, 191. (1959) 994-1002.

29. Zima, G. E. A Review of The Properties of Zircaloy-2, (1959).

30. Shober, F. R., Al, E., and Al., E. The Mechanical Properties of Zirconium and Zircaloy-2. BMI-1168 (1957).

31. Scott, P. B. Physical and Mechanical Properties of Zircaloy -2 and -4, Vol. 3269, (1965).

32. Garrison, B., Yan, Y., and TerMaath, S. "Determining failure properties of as-received and hydrided unirradiated Zircaloy-4 from ring compression tests." Engineering Failure Analysis, Vol. 125, (2021).

33. Bouffioux, P., and Rupa, N. "Impact of Hydrogen on Plasticity and Creep of Unirradiated Zircaloy-4 Cladding Tubes." Zirconium in the Nuclear Industry: Twelfth International Symposium, 399–420, (2000).

34. Pan, Z., Wang, N., and He, Z. "Measurements of Elastic Modulus in Zr Alloys for Candu Applications." 11th International Conference on CANDU Fuel, CW-128700-CONF-001, (2010).

35. Le Saux, M., Besson, J., Carassou, S., Poussard, C., and Averty, X. "A model to describe the anisotropic viscoplastic mechanical behavior of fresh and irradiated Zircaloy-4 fuel claddings under RIA loading conditions". Journal of Nuclear Materials, Vol 378, (2008).

36. Schwenk, E. B., Wheeler, K. R., Shearer, G. D., and Webster, R. T. "Poisson's ratio in zircaloy-4 between 24° and 316°C," Journal of Nuclear Materials, Vol 73, (1978).

37. Whitmarsh, C. L. Review of Zircaloy-2 and Zircaloy-4 Properties Relevant to N.S. Savannah Reactor Design. ORNL-3281, (1962).

38. Balourdet, M., and Bernaudat, C. Tensile Properties of Irradiated Zircaloy 4 Cladding Submitted to Fast Transient Loading. Proceedings of the CSNI Specialist Meeting, (1995).

39. Guo, W., Li, G., Yuan, F., Han, F., Zhang, Y., Ali, M., Ren, J., and Yuan, G. "Texture development and mechanical behavior of Zircaloy-4 alloy plates fabricated by cold rolling and annealing." Materials Science and Engineering, Vol. 807, (2021).

40. Deng, S., Song, H., Liu, H., and Zhang, S. H. "Effect of uniaxial loading direction on mechanical responses and texture evolution in cold pilgered Zircaloy-4 tube: Experiments and modeling." International Journal of Solids and Structures, vol. 213, (2021).

41. Mozzani, N., Auzoux, Q., Le Boulch, D., Andrieu, E., Blanc, C., Scott, C. P., and Barnel, N. "Mechanical behavior of recrystallized Zircaloy-4 under monotonic loading at room temperature: Tests and simplified anisotropic modeling." Journal of Nuclear Materials, Vol. 447, (2014).

42. AZOMaterials. Zircaloy-4(Alloy Zr4) (UNS R60804). https://www.azom.com/article.aspx?ArticleID=7644, (2022).

43. Daum, R. S., Majumdar, S., Tsai, H., Bray, T. S., Koss, D. A., Motta, A. T., and Billone, M. C. "Mechanical Property Testing of Irradiated Zircaloy Cladding Under Reactor Transient Conditions." ASTM Special Technical Publication, Small Spec, (2002).

44. Huang, J. H., and Huang, S. P. “Effect of hydrogen contents on the mechanical properties of Zircaloy-4.” Journal of Nuclear Materials, Vol. 208, (1994).

45. Tung, H. M., Chen, T. C., and Tseng, C. C. “Effects of hydrogen contents on the mechanical properties of Zircaloy-4 sheets.” Materials Science and Engineering, Vol 659, (2016).

46. Kamerman D., Cappia F., Wheeler K., Petersen P., Rosvall E., Dabney T., Yeom H., Sridharan K., Sevecek M., Schulthess J., “Development of axial and ring hoop tension testing methods for nuclear fuel cladding tubes” Nuclear Materials and Energy, Vol 31, (2022).

47. Hayes, T.A., Kassner, M.E. Creep of zirconium and zirconium alloys. Metal Mater Trans A, Vol 37, 2389–2396 (2006). https://doi.org/10.1007/BF02586213

48. Griffiths M. “A review of microstructure evolution in zirconium alloys during irradiation” *Journal of Nuclear Materials* Vol 159, (1988)

49. Daum R. S., Hydride-Induced Embrittlement of Zircaloy-4 Cladding Under Plane-Strain Tension A Thesis in Materials Science, The Pennsylvania State University (2007)

50. Raynaud P.A., Koss D.A., Motta A.T., “Crack growth in the through-thickness direction of hydrided thin-wall Zircaloy sheet” Journal of Nuclear Science and Engineering, Vol. 420 (2012)